Ocean Engineering 160 (2018) 78–93

Contents lists available at ScienceDirect

Ocean Engineering

journal homepage: www.elsevier.com/locate/oceaneng

A comparative DES study of wake vortex evolution for ducted and non-ducted propellers

Jie Gong, Chun-yu Guo *, Da-gang Zhao, Tie-cheng Wu, Ke-wei Song

College of Shipbuilding Engineering, Harbin Engineering University, Harbin, 150001, China

ARTICLE INFO

Keywords:
DES
Vortex evolution
Secondary vortices
Shear layer vortices
Characteristic frequency

ABSTRACT

A comparative numerical analysis was conducted on the evolution of wake vortices generated by ducted and non-ducted propellers in open-water tests. The simulations employed detached eddy simulation (DES) method with a focus on the detailed analysis of the composition of vortices and spatial evolution mechanism under various loading conditions. Compared with non-ducted propellers, the interference between the duct and the propeller directly changed the morphology of vortices and wake contraction, altered the energy distribution in the internal flow fields and thereby strengthened the self- and mutual induction and accelerated the primary merging and grouping processes. The results indicated that the shear layer vortices shedding from the duct displayed a strong interaction with the distorted tip vortices in an irregular manner and ejected the secondary coherent structures. Numerous secondary vortices were observed during the transition regime of the dynamic evolution. Followed by the energy dissipation and instabilities in the wake vortices, the wake vortex structures gradually broke down. The spectra of kinetic energy (KE) analyses of the wake field quantitatively confirmed the evolution of wake vortical structures in the temporal domain. The ducted propellers possessed a characteristic frequency that corresponded to its shaft frequency, blade passing frequency (BPF) and their harmonics.

1. Introduction

Ducted propellers are capable of generating high levels of thrust and efficiently operating under heavy loads, and they are widely utilized in specialised vessels and marine dynamic positioning systems. Special propulsions for ships constitute an important category of rotating machinery. A thorough understanding of flow mechanisms of rotating machines is of vital importance as it offers fundamental details for the hydrodynamic performance prediction. Currently, researches in the field focus on the structural composition, disturbance, and instability mechanism of vortices in the wake fields of rotating machinery. It is verified that the dynamic structure of wake vortices significantly affects the oscillations of rotating systems and their radiated noise performance (Korkut and Atlar, 2012).

Several studies have investigated the wake vortices characteristics of different rotating machinery (Felli et al., 2006; Lignarolo et al., 2015; Okulov and Sorensen, 2007; Paik et al., 2007). Nowadays, researchers have reached a consensus on the composition of rotating-machine wake vortices. Conceptually, the wake vortex system of a conventional propeller with N blades comprises of N blade vortices and a hub vortex, in which the former includes a tip vortex, thin vortex sheet shed off the edge of the blade and root vortex. The thin vortex sheet connects the tip vortex with the hub vortex. Felli et al. (2011) provided a detailed description of self- and mutual induction between tip vortices in the wake of axisymmetric flows and determined that the evolution process of wake vortices is divided into three different regimes. Kumar and Mahesh (2017) discovered that in addition to interactions between tip vortices, interactions also occur between tip vortices and smaller vortices generated by the roll-up of the blade trailing edge wake in the near wake and that vortical structures gradually break up and diffuse into the far wake in the unstable regime.

Numerous experimental studies were performed on non-ducted propellers. For example, Di Felice et al. (2004) and Felli et al. (2006) studied the velocity, pressure, and distribution of turbulent kinetic energy in the blade and tip vortex sheets of a propeller (E779A) by using particle image velocimetry (PIV) and laser Doppler velocimetry (LDV) measurements. Their studies revealed that viscosity and diffusion lead to the gradual dissipation of vortex sheets that are shed off the blades, and the point at which the shed vortex sheets disappear corresponds to the starting point of the roll-up process from which the wake vortices subsequently evolve into the transitional regime. Felli et al. (2011) investigated propeller wake evolution of propeller E779A configured with different numbers of

* Corresponding author.
E-mail address: guochunyu_heu@outlook.com (C.-y. Guo).

https://doi.org/10.1016/j.oceaneng.2018.04.054
Received 19 June 2017; Received in revised form 29 March 2018; Accepted 16 April 2018

Nomenclature

D	propeller diameter[m]
q	isovalue of Q-criterion[s^{-2}]
R	propeller radius[m]
k	wavenumbers
n	propeller rotational speed [rps]
O-xyz	Cartesian coordinate system
ε	pitch(°)
ω_x	normalised axial vorticity ($Vorticity[i]/(Ux/D)$)
U_∞	advance speed in open water [m/s]
u, v, w	local velocity components[m/s]
U	local velocity magnitude [m/s]
Ux	local axial velocity [m/s]
Re	Reynolds number
J	advance coefficient (U_∞/nD)
ρ	fluid density [kg m^{-3}]

Abbreviations

T	non-dimensional period of revolution
URANS	Unsteady Reynolds-averaged Navier-Stokes equations
Δt	time step
DES	Detached Eddy Simulation
Ktp	propeller thrust coefficient
DPM	Ducted Propeller Model
Ktd	duct thrust coefficient
NPM	Non-ducted Propeller Model
Kq	torque coefficient
PSD	Power Spectral Density
$Vorticity[i]$	axial vorticity [s^{-1}]
BPF	Blade Passing Frequency

blades in a cavitation tunnel, in which different grouping mechanisms in the vortex structures were observed with changes in the number of blades.

Numerical simulations were also widely applied in studies on the wake vortices of non-ducted propellers. Morgut and Nobile (2012) discussed the effects of the type of grid and turbulence model on predicting propeller wake flow fields. Baek et al. (2015) numerically examined wake flow fields and 3-D vortical structures of a propeller (KP505) with different advance ratios by solving unsteady Reynolds-averaged Navier-Stokes (URANS) equations, and an empirical model to describe the radial trajectories of propeller tip vortices was constructed. Muscari et al. (2013) numerically simulated the wake of a propeller (E779A) via URANS and detached eddy simulations (DES), wherein they discovered that the latter was reliable in reproducing the complex vortex structures in the far wake. Additionally, Dubbioso et al. (2013) and Di Mascio et al. (2014) conducted simulations on the wake field characteristics and wake vortex evolution of E779A model propeller in oblique flows by using URANS and DES methods. They discovered that secondary vortices play an important role in the dynamic evolution of wake vortices. Furthermore, Mahesh et al. (2015) and Balaras et al. (2015) utilized large eddy simulations (LES) to perform high-fidelity numerical simulations on the characteristics of instabilities of the propeller wake.

Bhattacharyya et al. performed extensive studies on predicting ducted propeller performance from the model scale to full scale. They utilized computational fluid dynamics (CFD) in the design of the ducted propeller (Bhattacharyya et al., 2015) and systematically investigated the scaling approach and scale effects of the ducted propellers (Bhattacharyya et al., 2016a, 2016b). Gaggero et al. (2014) used the RANS method to perform numerical predictions on cavitating tip vortices in ducted propellers, and the meshing and refinement topology used in the study are highly valuable as a reference for numerical studies since they attempted to capture the details of the flow field. Recently, Go et al. (2017) investigated the effect of a duct on propeller performance, in which the duct was located in front of the propeller. The results revealed 3-D vortical structures originating from the propeller tip and complex wake fields, and found that the duct could affect the flow field in a different manner.

Propeller blade loads and geometrical models affect the evolution of wake vortices generated by non-ducted propellers. In the case of ducted propellers, the flow separation derived from the duct and interfering interactions of the vortices in the wake field constitute primary factors that determine the hydrodynamic performance of ducted propellers. Hence, the composition and evolutionary mechanism of wake vortices are significantly more complex in ducted propellers when compared to those in non-ducted propellers. Most previous studies focused on the overall hydrodynamic performance of ducted propellers. Hence, it is meaningful to perform a detailed study on the vortical structures of ducted propeller and its evolution in wake fields. Therefore, the present study performs a comparative analysis on the wake vortex characteristics of ducted and non-ducted propellers by using the DES approach. It overcomes the inherent weaknesses of the RANS method in the simulation of vortex structures. The study investigates the effects of the numerical method, grid resolution, and loading on the simulation of wake vortex structures. Furthermore, the evolutionary process (deformation, grouping, and diffusion) of wake vortices of both propulsion configurations are analysed. It is expected that the findings of the study will aid in expanding and enriching the collective understanding of the mechanistic aspects of the hydrodynamic performance of specialised rotating machines.

The objectives of the numerical study include the following aspects: 1) assessing the applicability of DES in capturing the dynamic evolution of complex wake vortices; 2) comparing the structural composition and evolutionary processes of the wake vortex structures of ducted and non-ducted propellers under the same working conditions; and 3) quantitatively determining evolutionary processes of wake vortices based on power spectral density (PSD) analyses on the kinetic energy (KE) of the wake fields. The study is organized as follows. Section 1 describes the theoretical background. Section 2 discusses the setting of numerical models and assesses the uncertainty of the numerical simulations. In Section 3, the structural composition and evolution of wake vortices of the two models are qualitatively and quantitatively analysed. This is followed by discussing the wake vortices differences between the DES and URANS methods in Section 4. Finally, the conclusions are detailed in Section 5.

2. Theoretical background

2.1. Mathematical models

The numerical simulations of the viscous flow field are performed by the integration of the RANS equation. The motion of incompressible Newtonian fluids is integrated with the continuity equation and momentum conservation equation (Wang et al., 2015) as follows:

$$\frac{\partial u_i}{\partial x_i} = 0 \tag{1}$$

$$\frac{\partial(\rho u_i)}{\partial t} + \frac{\partial}{\partial x_j}\left(\rho u_i u_j\right) = \frac{\partial p}{\partial x_j} + \frac{\partial}{\partial x_j}\left(\mu\frac{\partial u_i}{\partial x_j} - \rho\overline{u_i' u_j'}\right) + S_j \tag{2}$$

where u_i and u_j denote the time-averaged values of velocity components ($i, j = 1, 2, 3$), p denotes time-averaged pressure, μ denotes the dynamic viscosity coefficient, $\rho\overline{u_i' u_j'}$ denotes the Reynolds stress term, and S_j

denotes the generalised source term of the momentum equation.

The DES model corresponds to a mixed numerical model that combines the strengths of both RANS and LES methods. In all DES simulations, the Spalart - Allmaras one-equation turbulence model (Spalart and Allmaras, 1994) is employed to resolve turbulence structures in the wake. Given the advantage of low consumption of computational resources, the Spalart & Allmaras model is a highly robust method to compute complex flows. A brief description of the DES method based on the Spalart & Allmaras model is given below.

The turbulence viscosity ν_t is solved by setting an auxiliary variable $\tilde{\nu}$ as follows:

$$\nu_t = \tilde{\nu} f_{\nu 1} \tag{3}$$

$$\text{with } f_{\nu 1} = \frac{\chi^3}{\chi^3 + C_{\nu 1}^3}, \chi = \frac{\tilde{\nu}}{\nu} \tag{4}$$

where $C_{\nu 1}^3$ denotes a constant. The auxiliary variable evolves based on a convection-diffusion equation with production and destruction source terms as follows:

$$\frac{\partial \tilde{\nu}}{\partial t} + u_j \frac{\partial \tilde{\nu}}{\partial x_j} = \frac{1}{\sigma}\left\{\nabla\cdot[(\nu+\tilde{\nu})\nabla\tilde{\nu}] + C_{b2}|\nabla\tilde{\nu}|^2\right\} + C_{b1}[1-f_{t2}]\tilde{S}\tilde{\nu} - \left[C_{w1}f_w - \frac{C_{b1}}{\kappa^2}f_{t2}\right]\left(\frac{\tilde{\nu}}{d}\right)^2 + f_{t1}\Delta U^2 \tag{5}$$

In the above equation, the first term inside the curly bracket on the right-hand side (RHS) denotes the diffusion term while the second term induces propagation of the turbulent front in laminar regions. The next two terms in the RHS represent the production and destruction of turbulence, and the final term is used to trigger turbulence at specific locations. The various C terms and σ correspond to constants including the Von Kármán constant $\kappa = 0.41$; f denotes a function of the wall distance d_0; and $\tilde{S}$ denotes a function of d_0 and $S = \sqrt{\Omega_{ij}\Omega_{ij}}$, with Ω_{ij} corresponding to the rotation tensor.

A new wall distance $\tilde{d}$ is defined to distinguish the domains evaluated by RANS and LES (Spalart, 2009), and this sidesteps difficulties typically encountered in the use of LES for near-wall regions. The definition of $\tilde{d}$ is as follows:

$$\tilde{d} = \min(d_0, C_{DES}\Delta) \tag{6}$$

where C_{DES} denotes a constant and $\Delta = \max(\Delta_x, \Delta_y, \Delta_z)$, which corresponds to the largest cell size of the three dimensions. A more complete and detailed description of the DES method is available in Shur et al. (2008).

2.2. Numerical models

In this study, 3-D, viscous, incompressible, constant-density and unsteady simulations are performed in the study with aid of the sliding mesh technique to numerically study the open water performance of a ducted propeller. The finite volume based segregated flow solver of the STAR-CCM + CFD code is utilized to simulate the flow field characteristics of the wake generated by the ducted propeller under various advance coefficients.

In the DES simulation, the SIMPLE algorithm is adopted to solve the pressure-velocity coupling equation. Specifically, convection, diffusion, and time terms are discretised by using the 2nd order upwind scheme, central differencing scheme, and 2nd order implicit time discretisation, respectively. In the unsteady DES simulation, the Courant-Friedrichs-Lewy (*CFL*) condition is employed to balance the temporal and the spatial scales. The *CFL* number is defined as follows:

$$CFL = \Delta t \cdot |U| / \Delta\min \tag{7}$$

where U denotes the local velocity magnitude,and $\Delta\min = \min(\Delta_x, \Delta_y, \Delta_z)$. According to the minimum grid spacing, the determination of time-step size in DES simulations should satisfy the demands of CFL number <1.0.

3. Numerical set-up

3.1. Test case

The geometry of the studied ducted propeller used in a dynamic positioning system is shown in Fig. 1. The propeller is a constant-pitch ($\varepsilon = 0°$) 4-bladed propeller with a diameter $D = 0.240$ m. The blade sections at each radius are symmetrical airfoils to ensure the same forward and reverse operating loads. Principal particulars of the propeller model is listed in Table 1. The Wageningen 19A duct is integrated with a tip clearance of 2 mm. The numerical models are defined as ducted propeller model (DPM) and non-ducted propeller model (NPM) respectively, and the propeller geometries are the same in both models. The size of the computational domain, boundary conditions (not including the walls of the duct), grid topology, turbulence model, and working conditions set for the DES model are kept constant for both the ducted propeller model and non-ducted propeller model.

An O-xyz Cartesian coordinate system with the origin O located at the geometrical center of the propeller is built in the simulation. The positive direction of the x-axis is defined as the uniform inflow direction, while the positive directions of the y and z axes are determined by the right-hand rule. The computational domain is a cylinder with a diameter 8D, and extends 2D upstream and 8D downstream from the origin O, respectively. Mahesh et al. (2015) observed that setting the upstream distance as 2D can avoid confinement effects while not affecting the computation of the evolution of the propeller's wake. The computational domain is divided into static and rotating sub-domains. The boundary conditions of the computational domain are set as follows: the inlet and the outer boundary of the cylinder are both set to the velocity inlet; the outlet is set to the pressure outlet; and the surfaces of the propeller and the duct are set to the no-slip wall. The contacting surface between the static and rotating sub-domains is set as the interface (see Fig. 2) to enable the exchange and iteration of information between the two sub-domains.

All the parameters are defined as dimensionless quantities. The advance coefficient is defined as $J = U_\infty/nD$. Two advance coefficients corresponding to $J = 0.3$ and 0.5 are selected to allow a comparison of heavy and light loads. A constant rotational speed corresponding to $n = 11$ revolutions per second (RPS) is used, while the inflow velocity is adjusted to alter the physics condition. The fluid density is kept constant at $\rho = 997.56$ kg m^{-3}, and the Reynolds number is the same as that of the model experiment, i.e., $Re = 3.5$–3.6×10^5.

Based on the final discretisation of the mesh, the dimensionless rotational period and time step are set as $T = 2\pi$ and $\Delta t \approx 0.01745$, respectively, to satisfy the CFL <1.0 requirement. Each iteration

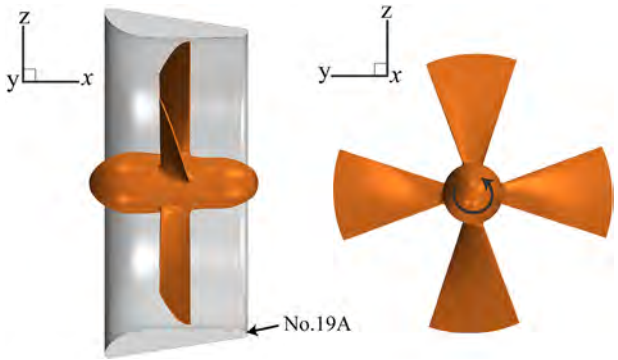

Fig. 1. Geometrical model of the ducted propeller.

Table 1
Principal particulars of the propeller model.

Propeller particulars	Value
Diameter D (m)	0.240
Radius R (m)	0.120
Hub ratio	0.190
Area ratio	0.417
Pitch ε (°)	0
No. blades	4

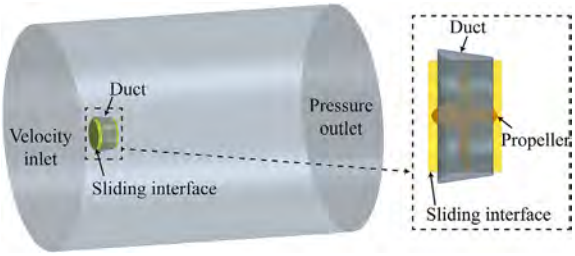

Fig. 2. Computational domain and interface.

corresponds to one degree rotation of the propeller with an inner iteration number of 10.

3.2. Mesh characteristics

A proper discretisation of the computational domain is extremely important to improve the accuracy of the numerical simulation. Hence, it is necessary to simultaneously consider the level of discretisation of the special regions of the ducted propeller during meshing. In theory, a sufficiently high grid density ensures a high resolution of the flow field. However, in the interim, it is also essential to minimise the number of cells for practical engineering applicability.

In the study, the rotational sub-domain is discretised by using a polyhedral mesh while the static sub-domain is discretised by using a trimmed mesh. As suggested in previous studies (Gaggero et al., 2014), eight prism layers meshes are arranged around the wall surfaces to better simulate the boundary layers of the propeller and the duct. To satisfy the requirements of the DES algorithm, the y^+ value of the walls is restricted to $y^+ < 1$.

It is necessary for the cell size of the computational domain to transition in a gradual manner to avoid numerical dissipations. The quality of unstructured mesh in regions of high curvature is relatively poor (for e.g., the tips of the blades and the leading and trailing edges of the blades), and thus it is necessary to discretise these regions at a finer level to improve the quality of the mesh. A surface remesher on the propeller and duct is executed to produce a high-quality surface mesh with good surface triangulation that is used to generate a mesh mixed by prism layer mesh and polyhedral or trimmed mesh. With respect to an unstructured grid system, several refinement volumes are employed in both sub-domains with different isotropic sizes as showed in Fig. 3. In the rotational domain, volume refinement (size = 1%D) is implemented in the annular cylindrical region of the blades' tips, while a gap refining region with an even finer grid size (size = 0.5%D) is employed in the gap between the blades' tips and the duct (shown in Fig. 3). The blade surfaces are refined along the feature lines of the leading and trailing edges (size = 0.1%D). In the static domain, two continuous tip vortex refining regions are established in the wake region to ensure an adequate grid density and to minimise the number of cells, with an isotropic size of 0.625%D and 1.25%D, respectively. Additionally, a hub vortex refining region is set up behind the hub to capture the formation and evolution of the hub vortex, and the relative size of the mesh is identical to that of the annular cylinder. The grid system is showed in Fig. 4. As previously illustrated, all the mesh parameters and refinement settings (with the exception of the duct of the DPM) for the NPM and DPM are identical In order to exclude the effects of the grid topology on the simulation results. The total number of cells of medium grid corresponds to 9.51 million while the static and rotational sub-domains account for 7.36 million and 2.15 million cells, respectively. For the fine grid, the geometric dimensions and locations of refinement volumes in the two sub domains are maintained as identical although they are scaled-down in the mesh size setting(for e.g., the isotropic size of the tip vortices refinement region equals to 0.5%D). The number of cells in the fine grid is 26.8 million with 9.6 million for the rotational domain and 17.2 million for the static domain.

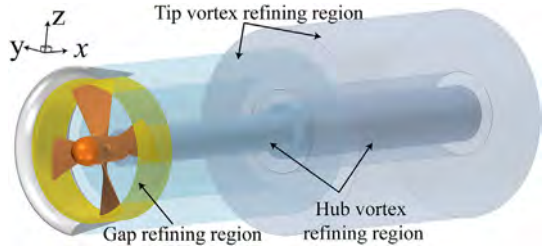

Fig. 3. Major mesh refinement regions.

3.3. Grid sensitivity verification

To assess the numerical uncertainty of the simulations, a suite of meshes are generated to quantitatively test the grid sensitivity, where $\Delta t/\Delta min$ is kept constant to ensure that the CFL number is also kept constant for all grid schemes. Based on the results of previous DES simulations (Muscari et al., 2013), the two-grid assessment procedure proposed by Roache (1997) is often used to evaluate grid sensitivity in these cases. The convergence analysis of the grid is usually performed using the hydrodynamic performance coefficients of the ducted and non-ducted propellers. In a manner similar to the disposal of the unstructured mesh in Baek et al. (2015), the refinement ratio r_0 was considered as a function of the total number of cells to uniformly refine the grid. The function is as follows:

$$r_0 = \left(\frac{N_{fine}}{N_{medium}}\right)^{1/d} \tag{8}$$

where N denotes the total number of cells in the grid and d denotes the dimensionality of the problem.

The error of the fine grid is estimated as follows:

$$E = \frac{f_2 - f_1}{1 - r_0^{p_0}} \tag{9}$$

where f_1 and f_2 denote the solutions on the fine and medium grids, respectively, r_0 denotes the mesh-refinement factor ($r_0 \approx \sqrt{2}$), and p_0 denotes the formal order of accuracy ($p_0 = 2$). The uncertainty is evaluated as follows:

$$U_N = Fs|E| \tag{10}$$

where F_S denotes a safety factor that is assumed as equal to 3.

Based on the results shown in Table 1, the U_N value of the duct thrust coefficient, Ktd, is considered as slightly excessive (5.79%) during the heavy loading, and it is expected that this is associated with the severe pulsations of the duct thrust under heavy loads. The results in Table 2 and Table 3 indicate that a considerably good agreement exists between the predicted and experimentally measured hydrodynamic performances of the DPM and NPM. The wake vortex prediction is considered as reliable. The uncertainty of the DPM and NPM results is always less than 3% when $J = 0.3$ and 0.5, respectively, and the numerical results obtained by using

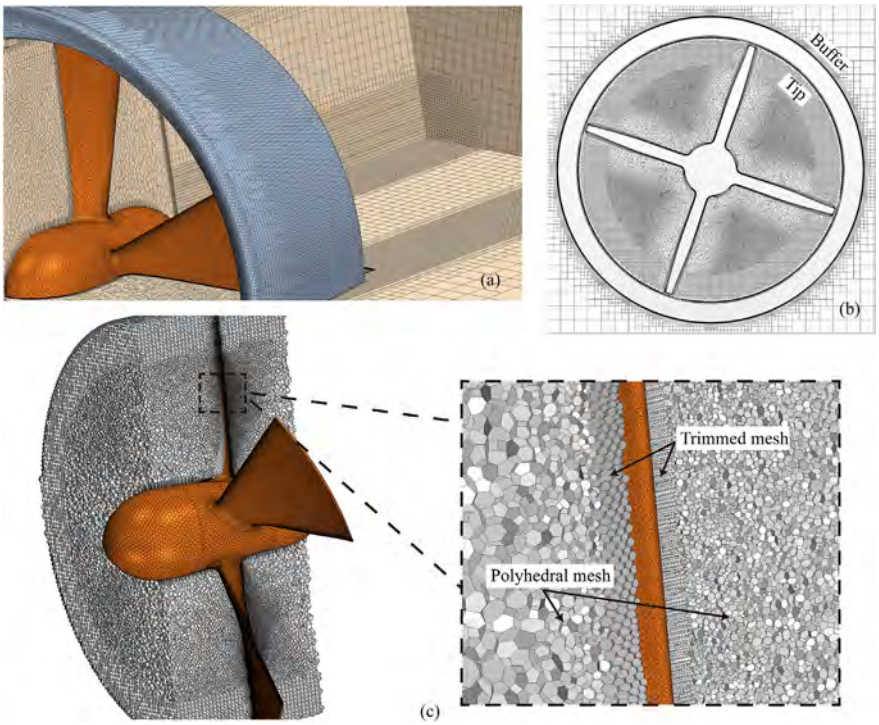

Fig. 4. Grid system: (a) longitudinal section view, (b) section view in the propeller plane, (c) hybrid volume mesh cells in rotational domain.

Table 2
Grid convergence analysis - DPM.

Load	Medium	Fine	E	Exp.	U_N (%)
$J = 0.3$					
Ktp	0.2034	0.2017	-1.7×10^{-3}	0.1985	0.86
Ktd	0.0791	0.0842	5.1×10^{-3}	0.0881	5.79
10*Kq*	0.3376	0.3379	3.0×10^{-4}	0.3401	0.09
$J = 0.5$					
Ktp	0.1571	0.1615	4.4×10^{-3}	0.1694	2.60
Ktd	0.0287	0.0289	2.0×10^{-4}	0.0269	0.74
10*Kq*	0.2855	0.2876	2.1×10^{-3}	0.2915	0.72

Table 3
Grid convergence analysis - NPM.

Load	Medium	Fine	E	Exp.	U_N (%)
$J = 0.3$					
Ktp	0.3126	0.3155	2.9×10^{-3}	0.3259	0.89
10*Kq*	0.4819	0.4866	4.7×10^{-3}	0.5026	0.94
$J = 0.5$					
Ktp	0.2213	0.2277	6.4×10^{-3}	0.2361	2.71
10*Kq*	0.3561	0.3632	7.1×10^{-3}	0.3648	1.95

medium and fine grids are very close. Furthermore, the calculated thrust and torque coefficients of the ducted propeller are compared with the experimental results (see Fig. 5) for the medium grid system with an extension to $J = 0.1$ and $J = 0.7$. For the perspective of thrust, torque and efficiency, the numerical prediction accuracy is acceptable for $J = 0.1$, 0.3 and 0.5, however, it performed more deviation for the highest advanced ratio $J = 0.7$. The deviation is related to the strong flow separation of the exterior side of the duct, downstream of the leading edge (Bhattacharyya et al., 2016a).

Additionally, for a typical DPM case ($J = 0.5$,physics time = 1s), with a medium grid number about 9.5 million, the accumulated CPU (Inter(R) Xeon(R) E5-2697 v2 @ 2.70 GHZ) time over 16 cores (32 processes/threads, parallel on local host) corresponds to 412,217 s (approximately 5 d) for 39,600 time-step. From the perspectives of mesh number and computational resource consumption, the medium grid is more applicable for practical applications. Therefore, all the subsequent analyses in the study are obtained from the medium grid simulations.

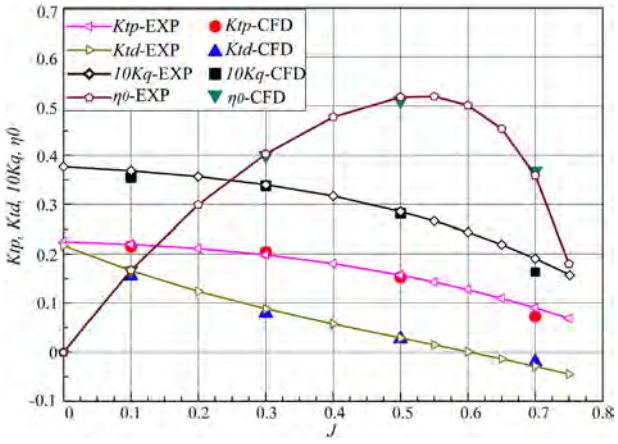

Fig. 5. Comparison of open water characteristics of the ducted propeller.

4. Results

4.1. Instantaneous wake fields

A significant difference exists between the distribution of vorticity and instantaneous induced velocity vectors in the longitudinal plane (x-z plane) of the wakes generated by the DPM and NPM. The instantaneous wake fields are analysed since the simulations reach numerical convergence and achieve a statistically steady-state regime. The standardised physical quantities in the longitudinal plane are described as follows: x and z axes are defined as x/R and z/R, respectively; the axial vorticity is standardised as ω_x=*Vorticity[i]/(Ux/D)*, relevant variables are included in the nomenclature list.

The initial velocity components (velocity at infinity) are subtracted from the wake field to yield the distribution of the instantaneously induced velocity vectors, and this provides an excellent representation of the propeller's perturbation on the flow field and the structural details of the perturbed flows. It can be seen from Tables 2 and 3 that the effective loading (Ktp and Kq) of the propeller under ducted condition is lighter than that of the non-ducted propeller for the same advance coefficient. A heavier effective loading of NPM induced stronger flow disturbances and results in a difference between local vortices and the velocity of the wake field. Under a heavy loading ($J = 0.3$), the power output from the propeller displayed a significant acceleration effect on the flow field. The wake acceleration region is in the $0 < z/R < 0.9$ range, in which the propeller strongly perturbs the wake flow and leads to the occurrence of continuous vortical structures in the instantaneous wake field (denoted by the round dashed circles in Fig. 6 (a) and (b)). These structures are distinct around the tips of the NPM although they are relatively indistinct around the DPM tips. This is related to the local scale of the vortices and the capture density of point vectors. Under a light loading ($J = 0.5$), the distribution of continuous vortical structures in the wake flow of the tip region ($z/R = 1$) is relatively regular. The gap between local vortex structures gradually increases when the vortices are convected downstream, and diffused towards the free-stream region ($z/R > 1$) as moving farther away. Additionally, the vortical structures are more tightly clustered in the NPM wake when compared to those in the DPM wake, and vortical structures are present within the hub vortex region of the NPM ($0 < z/R < 0.3$) in the $0 < x/R < 4$ region of analysis (the rectangular boxes as showed in Fig. 6 (b) and (d)).

By setting the same range of vorticity contours, the vorticity distribution patterns calculated for the NPM and DPM are compared in Fig. 7. Both models evidently display a tip vortex region ($0.8 < |z/R| < 1.1$), a blade shed vortex region ($0.3 < |z/R| < 0.8$), and a hub vortex region ($0 < |z/R| < 0.3$). Oval-shaped vorticity is continuously distributed in the tip vortex region, and the distribution of axial vorticities initially contracts and then diffuses outwards in the radial direction. In terms of the differences, the NPM wake fields exhibit a more organized distribution of vorticities in the tip vortex region when compared to that of the DPM. With a strong interference from the duct, the DPM displays a chaotic distribution of vorticity in the downstream region of the wake. Therefore, the results indicate that the NPM has a higher axial vorticity in the blade vortex shedding region and a higher level of hub vortex vorticity when compared to those of the DPM. The NPM also exhibits significant hub vortex oscillations after $x/R > 5$, while this does not occur for the DPM. Additionally, Fig. 8 shows the mesh density in the dashed rectangle named A region in Fig. 7 (a). It is observed that the mesh resolution is sufficient to capture the core of two adjacent tip vortices as well as the small-scale vortices.

4.2. Vortical structures

Based on the theories of vortex dynamics, the wake vortices of a propeller correspond to a typical coherent structures, and the characteristics of a wake field are determined by the generation, development, and destruction of the vortex structures and their complex interactions. The Q-criterion (Wu, 2013) is used here to help visualize the spatial structure of instantaneous vortices in the near wake field, and this essentially reconstructs the vorticity isosurfaces by setting q values. The Q-criterion q is defined as follows:

$$q = -\frac{1}{2}\left[\left(\frac{\partial u}{\partial x}\right)^2 + \left(\frac{\partial v}{\partial y}\right)^2 + \left(\frac{\partial w}{\partial z}\right)^2\right] - \left[\frac{\partial u}{\partial y}\frac{\partial v}{\partial x} + \frac{\partial u}{\partial z}\frac{\partial w}{\partial x} + \frac{\partial v}{\partial z}\frac{\partial w}{\partial y}\right] \tag{11}$$

To ensure a better illustration, the q values of the DPM are set to $q = 1000\ s^{-2}$. For the NPM cases, $q = 500\ s^{-2}$ and $3000\ s^{-2}$ are set for $J = 0.5$ and $J = 0.3$ respectively to visualize the spatial structures of wake vortices. Fig. 9 has visualized wake vortices (DPM, $J = 0.5$) and the envelope of the domain where the LES is model is active. It is observed that the LES model is activated in the wake region where the vortices are distributed.

The instantaneous 3-D wake vortex structures of the DPM and NPM exhibit distinct patterns under different loads and are illustrated in Fig. 10. With respect to the NPM, the patterns of its vortical structures are similar to those observed by Felli et al. (2011). The structures of the tip vortices, root vortices, and hub vortex are highly distinct, and the trajectories of the tip vortices generated by different blades exhibit clearly defined helical shapes (Fig. 10 (b) and (d)). An increase in the loading ($J = 0.3$) increases the strength of the tip vortices and promotes self- and mutual induction between adjacent tip vortices. This results in the early onset of merging and grouping during the evolution of tip vortices in the near wake field.

In comparison, the DPM vortical structures are more ambiguous since the presence of the duct alters the distribution of tip vortex energy in the internal flow field. Additionally, a shear layer flow emerges when the viscous fluid passes the surface of the duct, and this causes the shedding of several vortex structures from the trailing edge of the duct. Hence, the DPM wake flow is perturbed by propeller-duct interactions and interactions between shedding vortices and blade vortices. The trajectories of tip vortices in the DPM near the wake field correspond to irregular helices (Fig. 10 (a) and (c)). Furthermore, it should be noted that several secondary vortical structures (red dotted circles in Fig. 10) are formed and wrapped around the tip vortex tubes under both loads for the DPM

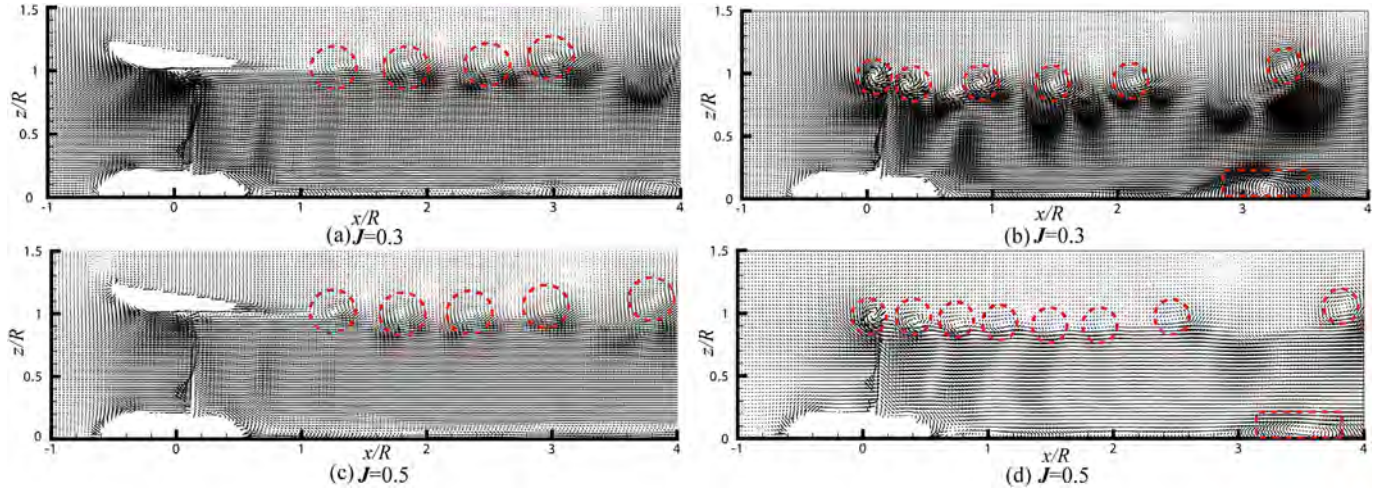

Fig. 6. Distribution of instantaneous velocity vectors in longitudinal plane for the DPM and NPM under different loads: a, c - DPM; b, d - NPM.

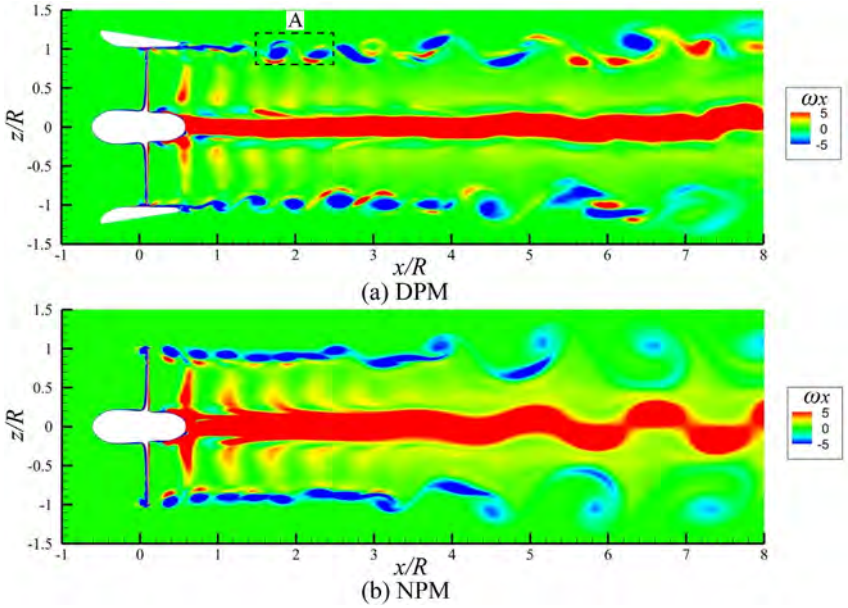

Fig. 7. Comparison between the instantaneous axial vorticity distribution of the DPM and NPM in the longitudinal plane; $J = 0.5$.

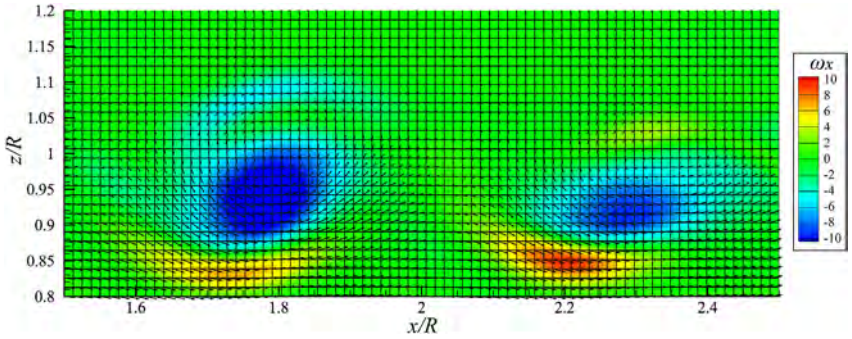

Fig. 8. Mesh density in the core of the tip vortices; DPM; $J = 0.5$.

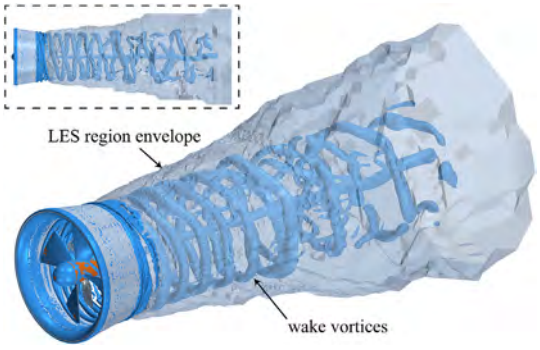

Fig. 9. LES domain and wake vortices in DPM for $J = 0.5$.

and especially for the heavy loading condition.

The magnitude of wake vorticity is illustrated by using volume rendering method that represents different colour gradations for varied spatial vorticity values. Based on each volume element of the volumetric data, the volume rendering method offers volume visualisation that overcomes the problems of the accurate representation of surfaces with respect to the isosurface techniques (Meiβner et al., 2000). It has advantages in the presence of weak or fuzzy features in the wake. The volume rendering method allows for a description of the magnitude of vorticity, as well as a better revealing the morphology of both small- and large-scale vortices. The following section discusses the characteristics and patterns of instantaneous vorticity distribution for the internal and near - far wake fields of the ducted propeller.

The vorticity distribution of the DPM internal flow fields under heavy loading is shown in Fig. 11 (a). The shed vortices, root vortices, and tip vortices possess distinct structures within the internal flow field. The interference between the duct and propeller directly induces deformation of the tip vortices and changes the energy distribution. The vortex distributions were important for the production of the thrust of the duct. A larger area of vortices distributing on the internal wall of the duct, and it enhances the circumferential flow around the duct surface that aids in recovering the vortex energy to improve propulsion efficiency (Oosterveld, 1970). Kumar and Mahesh. (2017) indicated that the blade geometry of the propeller affected the wake vortex due to the loads on the blade. Propellers with a slight skew and rake can potentially induce a stronger blade shed vortex.

The deformation of the tip vortex inside the duct was different as it developed downstream. Fig. 11 (b) - (d) show the changes using sketches of the core section of tip vortex. According to the theory of vortex dynamics (Wu et al., 2006), large vortices can be seen as a combination of numerous small vortex structures. It is concluded that the deformation of the tip vortex was caused by the blade-duct interaction and mutual induction of adjacent blades together. Two types of effects contribute to it: 1) Interaction of primary tip vortex and the boundary layer of the internal

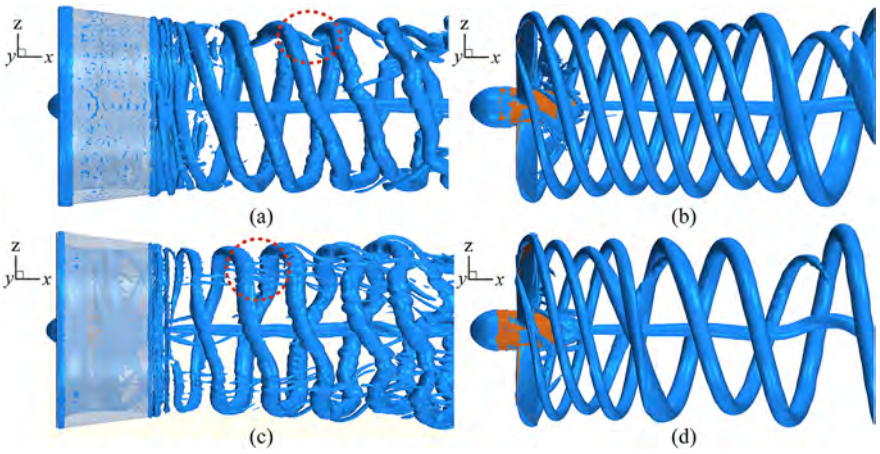

Fig. 10. Spatial structures of the instantaneous near-wake vortices that are constructed by using the Q-criterion: a, b - $J = 0.5$; c, d - $J = 0.3$.

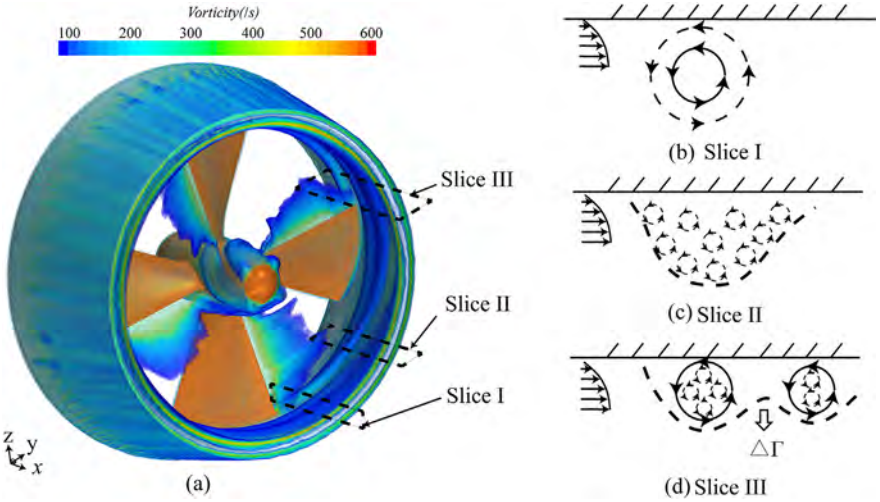

Fig. 11. Internal flow field characteristics of the DPM ($J = 0.3$) and sketches of the core section of the tip vortex: (b) Primary tip vortex in slice I; (c) Distorted vortex in slice II; (d) Sketch of the generation of two cores.

duct leads to the redistribution of tip vortex energy, resulting in a distorted circle in the cross section of the core (Fig. 11 (b) to (c)). 2) Mutual induction of adjacent blades strengthened the expansion of the tip vortex in the flow direction. The variable circulation of the tip vortices is closely related to the presence of the shed vorticity (Di Mascio et al., 2014) and partial circulation $\Delta\Gamma$ of the vortex ring is transferred to the blade shed vortex (see Fig. 12). The energy transfer path resides near the center of the spiral tip vortex, and the energy in the core is gradually distributed non-uniformly near the internal surface of the duct. Finally, the local vortex aggregation formed two separate cores from the original one core (Fig. 11 (d)). These features are significantly different from the characteristics of the non-ducted propeller tip vortices' behaviors.

The volume rendering of instantaneous vorticities of the near - far wake fields of the ducted propeller under heavy loads is shown in Fig. 13. As shown in the figure, the wake of a ducted propeller is composed of blade vortices, hub vortex, shear-layer vortices of the duct, and secondary vortical structures. Specifically, the blade vortices include tip vortices, root vortices, and the blade shed vortices, and the secondary vortical structures wrap around adjacent tip vortices.

Fig. 14 shows the spatial structures of the DPM wake vortices by using two different methods of visualisation, namely volume rendering and Q-criterion isosurface. The volume rendering method presents the small-scale structure of the secondary vortices more clearly while the Q isosurfaces better demonstrate the distortion of the tip vortex structures,

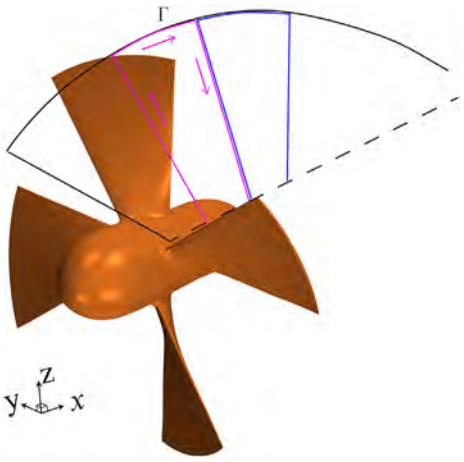

Fig. 12. Schematic representation of shed vorticity production and energy transport.

although they can only partially reveal the structure of the secondary vortices and vortex breakdown. Based on the findings of Di Mascio et al. (2014), the following three stages exist in the evolution of the wake

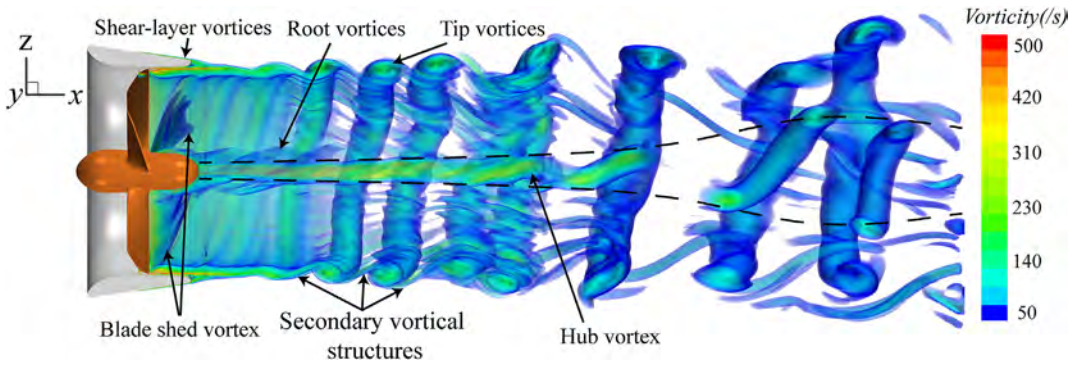

Fig. 13. Illustration of the instantaneous vorticity distribution of the DPM wake field and the wake vortex structures; $J = 0.3$.

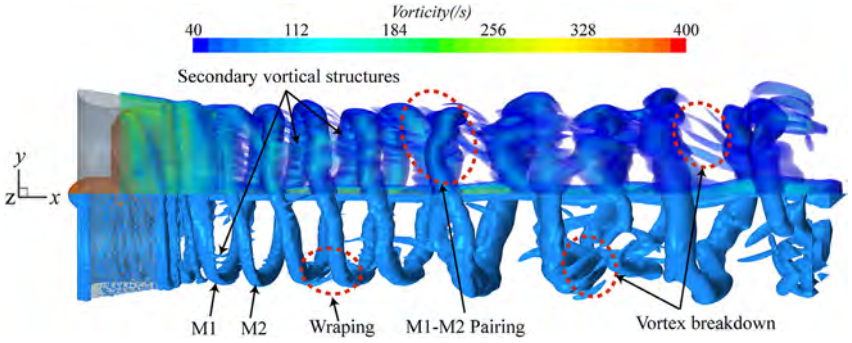

Fig. 14. Composition and evolution of the DPM wake vortices as illustrated by using two different visualisation methods; $J = 0.3$.

vortices of an open propeller: stable, transition and unstable regimes. The appearance of secondary vortical structures between the adjacent tip vortices marks the beginning of the transition regime. However, the presence of the duct alters the energy distributions inside the duct, and this causes the deformation of the tip vortices and accelerates the initial onset of vortex pairing process. Interference also occurs between the duct shear layer vortices and blade vortices, and there is no stable zone can be observed in the dynamic evolution of the DPM wake vortices.

The essential evolutionary process of DPM wake vortices is as follows. First, within the duct, the blade-duct interaction and mutual induction of adjacent blades lead to the deformation of the tip vortices, and energy transfer to the blade shed vortex strengthens the self- and mutual induction in return. However, the merging of tip vortices does not occur inside the duct. Then, the merging of tip vortices is happening as they are shed from the trailing edge of the duct. The shear layer vortices shedding from the external surface of the duct also has a strong interaction with the distorted tip vortices in an irregular manner. The vorticity is recognized in the secondary coherent structures as it ejected from the interaction. (Muscari et al., 2017). So, the merged tip vortex tubes (M1 and M2 in Fig. 14) and secondary vortices, which manifested as sheets that envelope the tip vortices, are observed in the near-middle wake field. Furthermore, numerous secondary vortical structures are developed and wrapped around two adjacent tip vortices as bridges, showing the energy accumulation and transport in the middle-far field. Finally, the interference between different vortices becomes increasingly complex as it convected downstream, vortex structures gradually break down and diffuse, and the hub vortex oscillations are observed by its trajectory variations (the dotted lines in Fig. 13 illustrate the envelope of the hub vortex oscillation) in the downstream region.

4.3. Kinetic energy spectra

4.3.1. PSD analysis for DPM and NPM

The characteristics of kinetic energy spectra in various locations are correlated with the local morphology of the wake. Felli et al. (2011) analysed the energy transfer process in the wake field by using the PSD analysis of KE in which the kinetic energy was defined as $KE = 0.5(u^2+v^2+w^2)$.

Based on the transient pressure field, the core position of the tip vortices is identified at the center of low pressure. Similar approach was used in Balaras et al. (2015), which showed in detail the wake contraction of a submarine propeller. Instantaneous locations of tip vortex core and approximate tracks of tip vortices are illustrated in Fig. 15. The core of tip vortices are marked by red rings and the vortices trajectory are indicated by the thick dash lines approximately. This reveals an apparent difference in the wake contraction behaviors between DPM and NPM

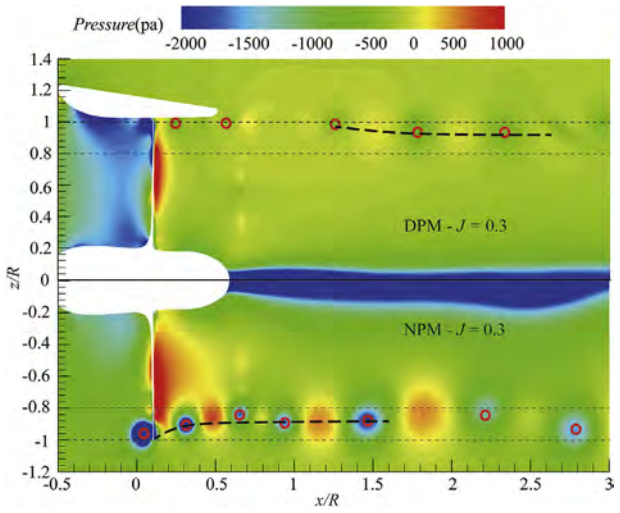

Fig. 15. Instantaneous locations of the tip vortex core and approximate tracks of the tip vortices in the near wake for $J = 0.3$ (top, DPM; bottom, NPM).

cases. As showed in the NPM case (Fig. 15, bottom) that the wake contraction is observed immediately downstream of the propeller plane with a high slope of the wake radius. The trajectory in the radial direction reaches around 0.9R after $x/R = 0.5$ and keeps stable in the wake. On the other hand, the duct has obviously delayed the wake contraction since the contraction occurs near $x/R = 1.2$ in the DPM case.

A schematic of the layout of probing points set in the wake field is showed in Fig. 16. To keep the probing points locating near the track of the tip vortices, probing points P_i ($i = 1$–8) are set up at non-equidistant intervals within the 4*D* range downstream of the NPM wake, at $z/R = 0.9$ in the radial direction and $x/R = 0.5$, 1.0, 1.5, 2.5, 3.5, 4.5, 6.0, and 8.0 in the axial direction as recommended by Di Mascio et al. (2014). For the DPM cases, eight probes are located in the same axial locations with the NPM cases. However, P_1 and P_2 are located at $z/R = 0.95$ in radical direction where is closer to the tip vortices trajectory. The distribution of other probing points is in accordance with the NPM cases in the radical direction. Furthermore, additional three probes (P_9, P_{10}, P_{11}) are located in the hub vortex region ($z/R = 0$) with the axial distances $x/R = 1.5$, 3.5 and 6.0.

To improve the legibility of the figures to be shown below, the forementioned probing points mentioned are divided into three groups, namely the near field (P_1, P_2, P_3), middle field (P_4, P_5, P_6), and far field (P_7, P_8). The wavenumber, *k*, is standardised based on the blade passing frequency (BPF), i.e., the BPF corresponds to $k = 1$, while the shaft frequency corresponds to $k = 0.25$.

The KE fluctuations and PSD analysis of KE for DPM and OPM are compared and analysed for the case at $J = 0.5$ in the following part. The average KE levels are represented by the lines and the maximum and minimum values are showed by points in Fig. 17. It is noted that the average KE levels are higher in P_1 than in P_2 and P_3 in the near field. The blade has induced stronger velocities in the nearest probing point. The average KE level of the wake gradually increases from the near field to the far field over time for both models. Additionally, KE fluctuations with larger amplitudes are observed in the middle field of NPM when compared to those in the DPM. The fluctuations in the middle field also exceed those in the rest of the wake since the interference between vortices in this region results in the unstable propagation of the KE.

A comparison of the PSD characteristics of both models at $J = 0.5$ indicates that the spectral features of both models exhibit a few similarities: 1) in the low-frequency range, the spectral characteristics show significant variations, and decline rate of the power density decreases when the k value increases; 2) the negative slope in the low-frequency range becomes steeper for P_4 - P_6 points when compared to P_1 - P_3; and 3) from the near field to the far field, the leading frequency gradually shifts towards the shaft frequency ($k = 0.25$) gradually. These characteristics are consistent with the results of previous studies (Di Mascio et al., 2014; Felli et al., 2011).

Conversely, significant differences exist between the PSD spectra of the NPM and DPM with respect to their low-frequency and high-frequency. As showed in Fig. 18, peaks continuously appear at the BPF and its harmonics in the NPM wake and they are also observed at the BPF of the DPM, but reduced in the amplitude. In addition, peaks are observed at the shaft frequency and its harmonics for the DPM and the signal attenuation of DPM evidently exceeds that of NPM.

In the near, middle and far fields of the NPM, viscous dissipation causes the spectral averages of P_1 to P_3 to rapidly decrease because the interference between the adjacent tip vortices is very strong due to the short gaps between them. In the middle field, peaks are clearly observed throughout the entire frequency range and fewer regions gradually undergo intense attenuation. In the far field, peaks occur at the harmonics of the shaft frequency.

With respect to the DPM, the complex interference between multiple types of vortices around the trailing edge of the duct leads to significant fluctuations in the spectral characteristics of P_1 over the entire frequency range. However, clear peaks are also observed in BPF and its multiples in the near field. In the middle field, a characteristic wavenumber k is not observed in the low-frequency range ($k < 5$), while the signal rapidly declines in the high-frequency range. From the middle field to the far field, significant peaks are not observed in the mid-to-high frequency range, and the signal level after $k > 5$ gradually approaches the white noise level.

Additionally, the kinetic energy spectra in eight positions are collected for the DPM under two loading conditions (Fig. 19). It is clearly observed that the peaks at the harmonics of BPF are basically the same in the low-frequency region in the near fields (P_1 to P_3). However, the mean value of the spectra decreases in P_4 in the mid-to-high frequency region for $J = 0.3$ while a similar rule is observed in P_5 at $J = 0.5$. Since the high loaded condition could induce stronger interaction between adjacent vortices, the grouping process occurred earlier than the light loaded conditions and resulted in the acceleration of energy dissipation.

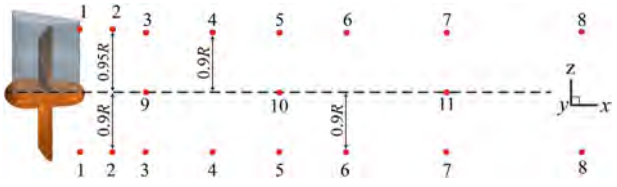

Fig. 16. Schematic of the layout of probing points set in the wake field.

4.3.2. PSD characteristics and morphology of wake vortices

With the aim of exploring the direct correlation between the spectral characteristics of the KE and the morphological evolution of the local wake vortices, the PSD characteristics of the DPM and NPM wake fields under $J = 0.3$ and $J = 0.5$ are further analysed to examine their correspondence to the wake vortex evolution in the near, middle, and far fields, respectively. The evolution process of tip vortices is analysed at

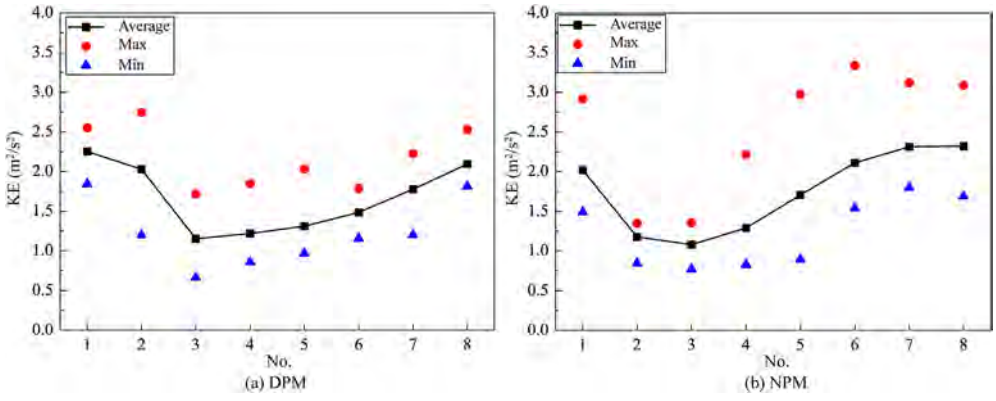

Fig. 17. KE fluctuations of the DPM and NPM ($J = 0.5$) in the time domain.

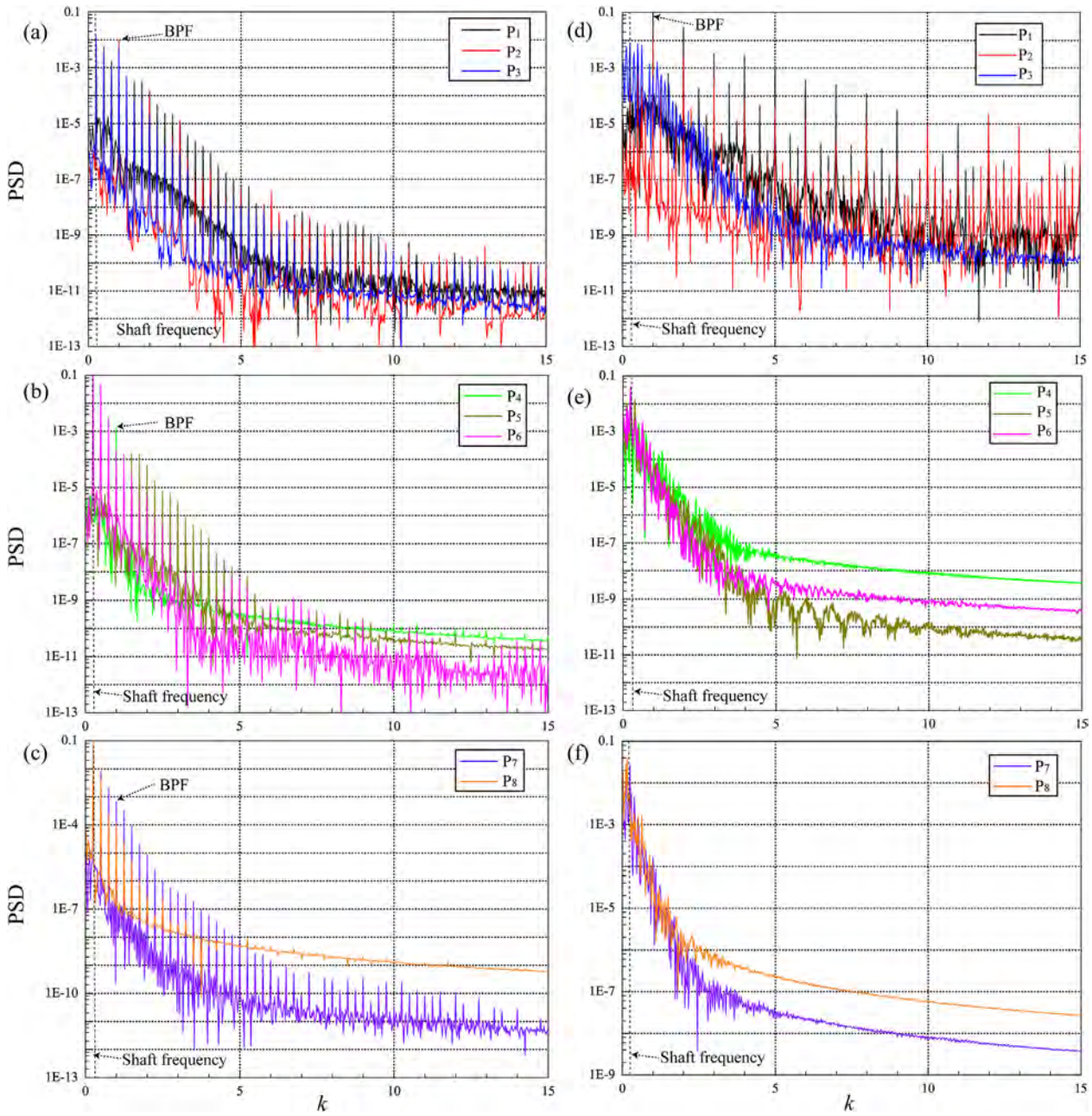

Fig. 18. PSD of kinetic energy; $J = 0.5$; (a, b, c) - NPM, (d, e, f) - DPM.

probe points P_3, P_5, and P_7 and the PSD analysis of hub vortex evolution is carried out at probes P_9, P_{10}, and P_{11}. This aids in quantitatively revealing the evolutionary mechanism of wake vortices. The morphology of the wake vortices is represented by using the Q-criterion. The isosurface parameter is set as $q = 1000\ s^{-2}$and $q = 500\ s^{-2}$ to optimise the expression of the structural morphology of the wake vortices.

In the heavy loading case of the DPM (Fig. 20), peaks corresponding to the shaft frequency, blade frequency and their harmonics ($k = 0.5$, 0.75, …and $k = 2$, 3, …) appear in the low-frequency range at P_3, P_5, and P_7. Based on the findings of Muscari et al. (2013), a non-integer k indicates that pairing occurs between tip vortices. As indicated by the wake vortex structures of the DPM, pairing and grouping occurred as early as those in the tip vortex structures inside the duct. With respect to a typical 4-bladed propeller, recognizable tip vortex structures in the outflow of the duct are already grouped into two adjacent vortex tubes (M1 and M2, Fig. 14). This results in a distinct peak at $k = 0.5$ for P_3. Additionally, P_5 corresponds to the self- and mutual induction locations, where several secondary vortical structures exist. The $k = 0.75$ peak is related to the rapid attenuation of primary vortices and the strengthening of secondary vortices at this point. The original morphology of the wake vortices is increasingly distorted, and thus the leading frequency gradually shifts towards the shaft frequency of $k = 0.25$. Furthermore, P_7 corresponds to the location of tip vortex re-grouping in which enhanced instability of the wake vortices leads to vortex breakdown and promotes the energy diffusion. Consequently, $k = 0.25$, $k = 0.5$, and $k = 0.75$ peaks gradually decline towards the far field, and a maximum peak appears at $k = 0.25$ for the far-field probe. Similar features are also observed in the analysis of tip vortices region for $J = 0.5$ case (Fig. 21).

The evolution process of the hub vortex in the wake is illustrated in the PSD analysis for probes P_9, P_{10}, and P_{11} as showed in Figs. 20 and 21. The results indicate that the harmonic frequency is related to the shaft frequency and multiple of shaft frequency. Peaks are observed in the $k = 0.25$, 0.5 and $k = 0.75$ at P_9 and P_{10}. With the diffusion of the hub vortex energy, peaks are smoothed in multiples of the shaft frequency in

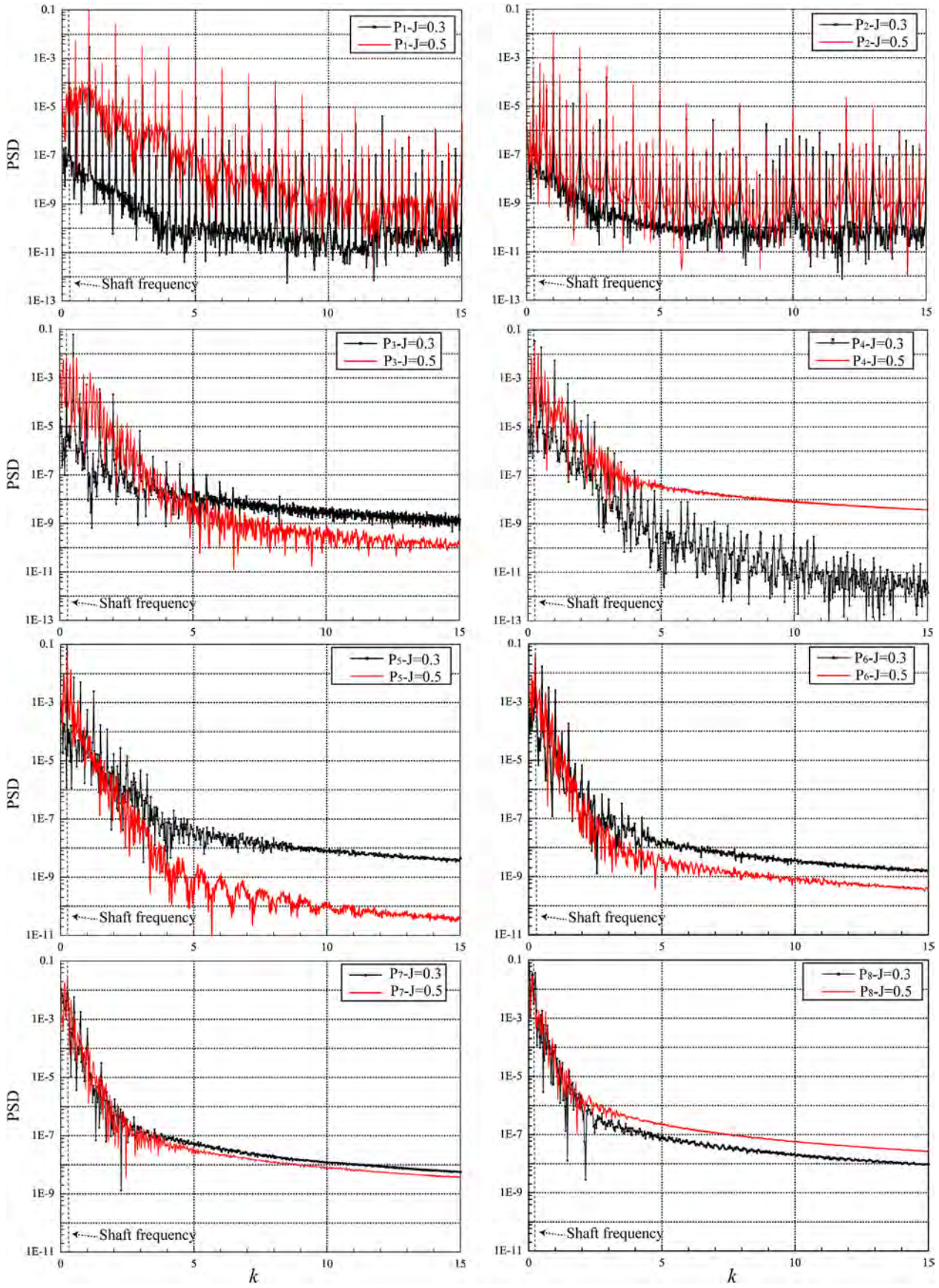

Fig. 19. Comparison of kinetic energy spectra of DPM for $J = 0.3$ and $J = 0.5$.

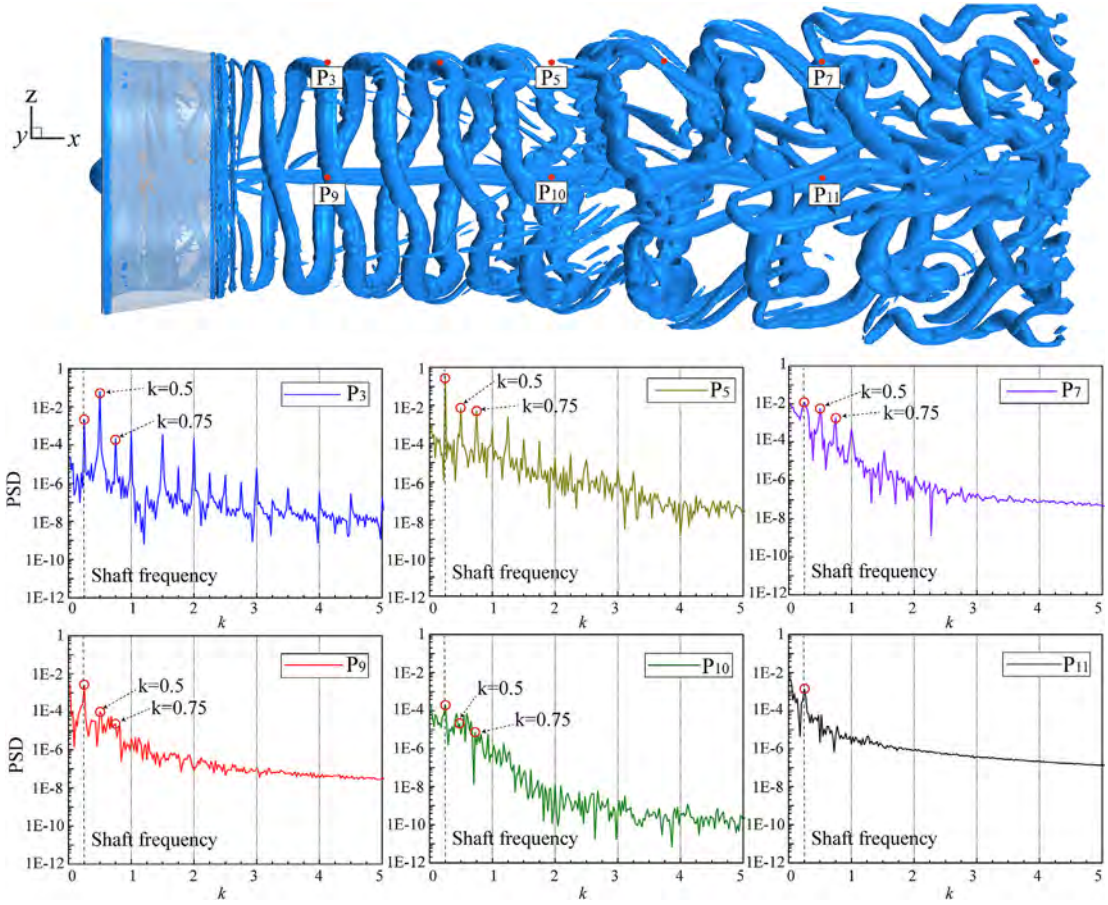

Fig. 20. PSD at probes P_3, P_5, P_7, P_9, P_{10}, and P_{11}; $J = 0.3$; DPM.

the far field (at P_{11}). It is noted that the spiral trajectory of hub vortex arose near P_{10} under heavy loading conditions (Fig. 20). The oscillation is related to the instability of hub vortex and it causes strong interactions between hub vortex and tip vortices (Kumar and Mahesh, 2017). It is observed that the signal fluctuates drastically and decreases rapidly in the low-frequency range ($k < 5$).

As shown for the NPM cases (Fig. 22), peaks can be observed in the low-frequency range at the BPF and its harmonics ($k = 1, 2, \ldots$), as well as at the non-integer multiples of k ($k = 0.5,\ 0.75,\ \ldots$) apparently. The appearance of these characteristic frequencies is directly related to the evolutionary characteristics of the NPM wake vortex structures. The clear $k = 0.5$ peak at P_3 indicates that secondary vortical structures begin to appear in the near wake field. The pairing of tip vortices is initiated although the process is yet to be completed at this point. Where, P_5 probe is located at the end of the first pairing process, and from this an increase in the $k = 0.5$ peak is observed. Additionally, an increase in the $k = 0.75$ peak occurs when the transition zone of the wake flow continues to develop. P_7 probe is located within the region where the second pairing process of the wake vortices occurs. The rapid weakening of the primary vortices and the strengthening of the activity of secondary vortices lead to an increase in $k = 0.75$.

Moreover, the structure or strength of these secondary vortex structures is not captured in Fig. 22 due to the resolutions of the grid. This implies that the smallest grid size in the previously described meshing process of the DPM (0.625% D) is not sufficient to capture the secondary vortical structures of the NPM.

5. Discussions

Wake vortex structures that are separately obtained by using DES and URANS are compared to verify the superiority of the DES method in the simulation of small scale wake vortex structures. To ensure an objective comparison, only the computational method is changed while the remaining physical parameters and meshing topologies are maintained as identical. The instantaneous vorticity computed by the DES and URANS methods in the near-wake field of the DPM for $J = 0.5$ is shown in Fig. 23. The DES simulation shows that the vortex structure composition in the near-wake field of the DPM is identical to that observed at $J = 0.3$, and the morphologies of the secondary vortices (indicated by the black dashed box in Fig. 23 (a)) are clear and distinct. Furthermore, the evolutionary process of the near-wake field vortices also qualitatively corresponds to the same as that described above. In the URANS simulation, the blade vortices (tip, root, and blade shed vortices) and the hub vortex are clearly resolved. However, the secondary vortical structure is not captured well in terms of local results. Additionally, significant differences are also observed in the vortex strengths on the cross section computed by DES and URANS. Therefore, the results indicate that the DES method achieves wake vortex modes and morphologies that are close to those that occur in reality albeit with a relatively higher computational cost. The results also suggest that a minimum grid size of 0.625% D in the wake is sufficient to reconstruct secondary vortices in the DPM wake.

6. Conclusions

In the study, DES simulations were carried out to analyse the composition, 3-D structure, wake contraction and evolution of wake vortices of DPM and NPM in a systematic and comprehensive manner. The structural characteristics of the DPM wake vortices were depicted in detail. A qualitative analysis of the instantaneous wake vortex structures

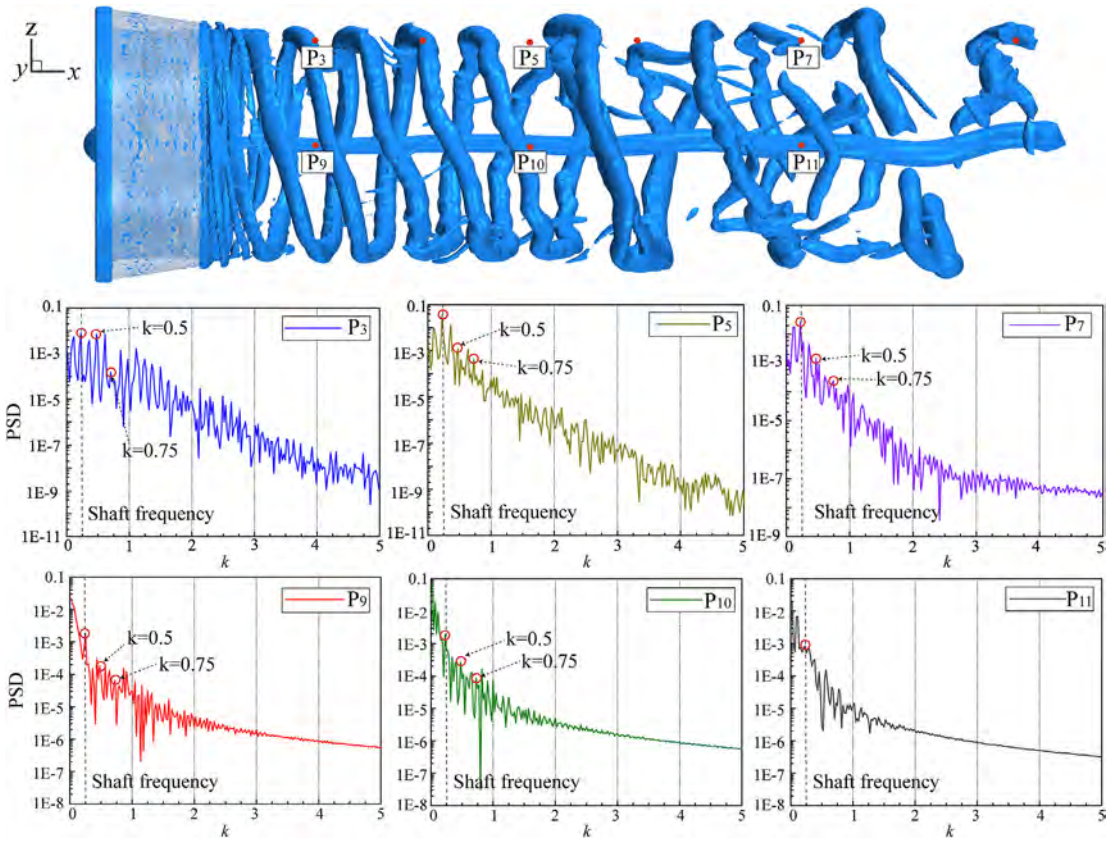

Fig. 21. PSD at probes P_3, P_5, P_7, P_9, P_{10}, and P_{11}; $J = 0.5$; DPM.

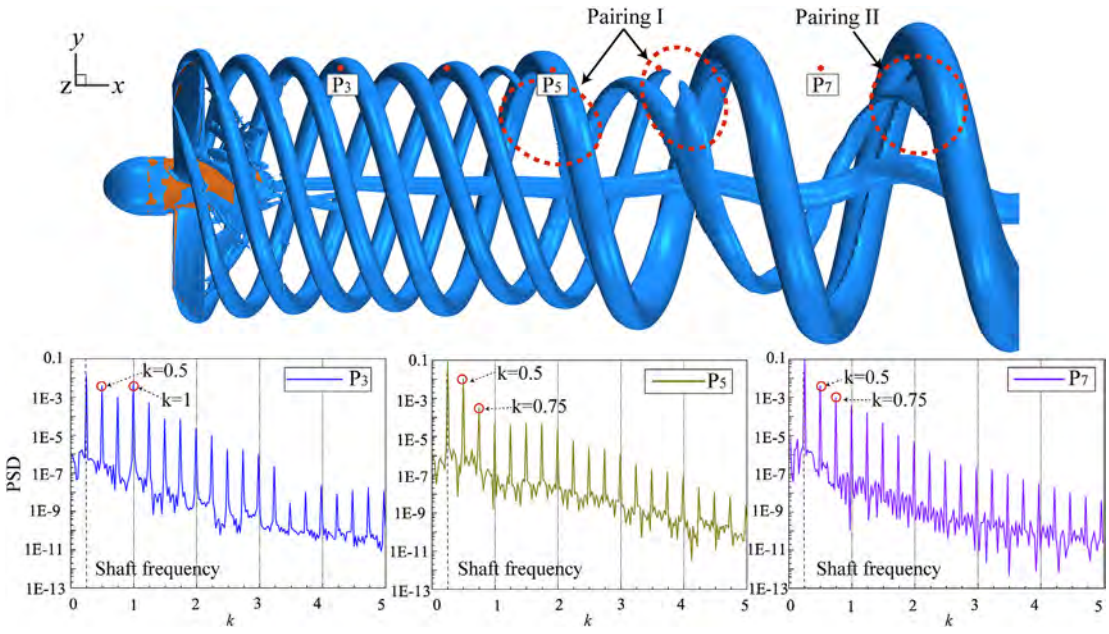

Fig. 22. PSD at probes P_3, P_5, and P_7; $J = 0.5$; NPM.

was performed by illustrating the 3-D structures and evolution of wake vortices, with the aid of Q-criterion and volume rendering methods. Additionally, multiple probing points were set up in the wake field to monitor the wake KE variation in the time domain. The PSD analysis of KE further quantitatively elucidated the complex interactions between various types of vortices and the corresponding changes in the wake field.

The numerical results reveal that the captured wake vortices as typical coherent structures in turbulence exhibit significant consistency with the results obtained by previous studies on NPM in terms of composition, structural evolution, and KE spectra characteristics. This validates the credibility of the numerical model in examining the evolution of wake vortices. The ducted propeller's wake vortex system was comprised of tip vortices, root vortices, blade shed vortices, a hub vortex, duct shear layer vortices, and secondary vortices. The interference

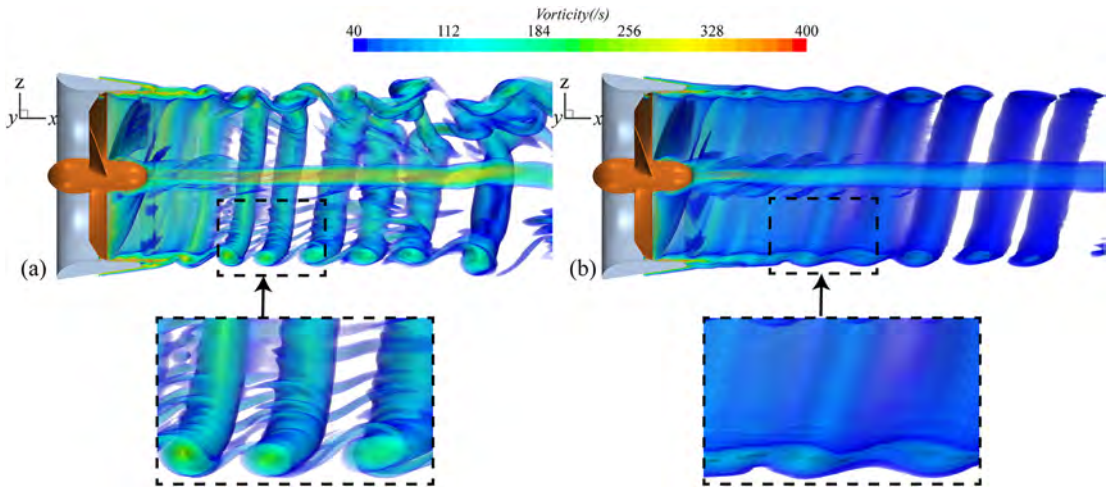

Fig. 23. Comparison of vorticity distribution for the near-wake field computed by DES and URANS for $J = 0.5$.

between the duct and the propeller has strengthened the self-induction effects and promoted the energy redistribution in the internal flow fields, which has led to the rapid merging and grouping of tip vortices at the trailing edge of the duct. Furthermore, the merging of shear layer vortices from the trailing edge of the duct and the outflowing tip vortices rapidly promoted the energy transfer and ejected the secondary coherent structures in the near wake field. Consequently, secondary vortices bridging consecutive tip vortices were observed as the deformed tip vortices convected downstream. The trajectory of the hub vortex commenced oscillating at the location at which the tip vortex grouping began to occur with an increasing amplitude moving downstream. Following this, the enhanced wake energy dissipation eventually led to the breakdown and diffusion of vortex structures.

Due to the existence of the duct, the wake contraction was delayed in the DPM cases. When compared with the NPM, the trajectory of tip vortices was observed at a larger distance in the radial direction with a low slope of the wake radius in the near field. The PSD analysis of the KE quantitatively described various forms of distortion that occurred during the evolution of instantaneous wake vortex structures from the energy transfer perspective. Through induced stronger interference and distortion in wake vortices, the KE spectra characteristics of the DPM demonstrated that peaks were observed corresponding to multiples of the BPF as NPM cases. Furthermore, peaks corresponding to the shaft frequency and its harmonics in the PSD constituted quantitative manifestations of tip vortex grouping and the development of secondary vortical structures in the DPM wake.

Acknowledgements

The study was supported by the National Natural Science Foundation of China (Grant Nos. 51709060, 51209048 and 51409063), the Equipment pre research project of china (Grant No. 41407010501), and in response to the significant support for the research project titled 'High technology Ship Scientific Research Project' (MIIT[2016]26) carried out by the Ministry of Industry and Information Technology.

References

Baek, D.G., Yoon, H.S., Jung, J.H., Kim, K.S., Paik, B.G., 2015. Effects of the advance ratio on the evolution of a propeller wake. Comput. Fluids 118, 32–43. https://doi.org/10.1016/j.compfluid.2015.06.010.

Balaras, E., Schroeder, S., Posa, A., 2015. Large-eddy simulations of submarine propellers. J. Ship Res. 59, 227–237. https://doi.org/10.5957/JOSR.59.4.150047.

Bhattacharyya, A., Krasilnikov, V., Steen, S., 2015. Scale Effects on a 4-bladed propeller operating in ducts of different design in open water. In: Fourth International Symposium on Marine Propulsors Smp'15, USA.

Bhattacharyya, A., Krasilnikov, V., Steen, S., 2016a. Scale effects on open water characteristics of a controllable pitch propeller working within different duct designs. Ocean. Eng. 112, 226–242. https://doi.org/10.1016/j.oceaneng.2015.12.024.

Bhattacharyya, A., Krasilnikov, V., Steen, S., 2016b. A CFD-based scaling approach for ducted propellers. Ocean. Eng. 123, 116–130. https://doi.org/10.1016/j.oceaneng.2016.06.011.

Di Felice, F., Di Florio, D., Felli, M., Romano, G.P., 2004. Experimental investigation of the propeller wake at different loading conditions by particle image. J. Ship Res. 48 (2), 168–190.

Di Mascio, A., Muscari, R., Dubbioso, G., 2014. On the waske dynamics of a propeller operating in drift. J. Fluid Mech. 754, 263–307. https://doi.org/10.1017/jfm.2014.390.

Dubbioso, G., Muscari, R., Di, A., 2013. Analysis of the performances of a marine propeller operating in oblique flow. Comput. Fluids 75, 86–102. https://doi.org/10.1016/j.compfluid.2013.01.017.

Felli, M., Di Felice, F., Guj, G., Camussi, R., 2006. Analysis of the propeller wake evolution by pressure and velocity phase measurements. Exp. Fluids 41 (3), 441–451. https://doi.org/10.1007/s00348-006-0171-4.

Felli, M., Camussi, R., Di Felice, F., 2011. Mechanisms of evolution of the propeller wake in the transition and far fields. J. Fluid Mech. 682, 5–53. https://doi.org/10.1017/jfm.2011.150.

Gaggero, S., Tani, G., Viviani, M., Conti, F., 2014. A study on the numerical prediction of propellers cavitating tip vortex. Ocean. Eng. 92, 137–161. https://doi.org/10.1016/j.oceaneng.2014.09.042.

Go, J.S., Yoon, H.S., Jung, J.H., 2017. Effects of a duct before a propeller on propulsion performance. Ocean. Eng. 136, 54–66. https://doi.org/10.1016/j.oceaneng.2017.03.012.

Korkut, E., Atlar, M., 2012. An experimental investigation of the effect of foul release coating application on performance, noise and cavitation characteristics of marine propellers. Ocean. Eng. 41, 1–12. https://doi.org/10.1016/j.oceaneng.2011.12.012.

Kumar, P., Mahesh, K., 2017. Large eddy simulation of propeller wake instabilities. J. Fluid Mech. 814, 361–396. https://doi.org/10.1017/jfm.2017.20.

Lignarolo, L.E.M., Ragni, D., Scarano, F., Simão Ferreira, C.J., van Bussel, G.J.W., 2015. Tip-vortex instability and turbulent mixing in wind-turbine wakes. J. Fluid Mech. 781, 467–493. https://doi.org/10.1017/jfm.2015.470.

Mahesh, K., Kumar, P., Gnanaskandan, A., Nitzkorski, Z., 2015. LES applied to ship research. J. Ship Res. 59, 238–245. https://doi.org/10.5957/JOSR.59.4.150049.

Meißner, M., Pfister, H., Westermann, R., Wittenbrink, C.M., 2000. Volume visualization and volume rendering techniques. Eurographics. https://doi.org/10.2312/egt.20001035.

Morgut, M., Nobile, E., 2012. Influence of grid type and turbulence model on the numerical prediction of the flow around marine propellers working in uniform inflow. Ocean. Eng. 42, 26–34. https://doi.org/10.1016/j.oceaneng.2012.01.012.

Muscari, R., Di Mascio, A., Verzicco, R., 2013. Modeling of vortex dynamics in the wake of a marine propeller. Comput. Fluids 73, 65–79. https://doi.org/10.1016/j.compfluid.2012.12.003.

Muscari, R., Dubbioso, G., Di Mascio, A., 2017. Analysis of the flow field around a rudder in the wake of a simplified marine propeller. J. Fluid Mech. 814, 547–569. https://doi.org/10.1017/jfm.2017.43.

Okulov, V.L., Sorensen, J.N., 2007. Stability of helical tip vortices in a rotor far wake. J. Fluid Mech. 576, 1–25. https://doi.org/10.1017/S0022112006004228.

Oosterveld, M.W.C., 1970. Wake Adapted Ducted Propellers, Doctoral Thesis. Delft University of Technology, Netherlands.

Paik, B.G., Kim, J., Park, Y.H., Kim, K.S., Yu, K.K., 2007. Analysis of wake behind a rotating propeller using PIV technique in a cavitation tunnel. Ocean. Eng. 34, 594–604. https://doi.org/10.1016/j.oceaneng.2005.11.022.

Roache, P.J., 1997. Quantification of uncertainty in computational fluid dynamics. Annu. Rev. Fluid Mech. 29, 123–160.

Shur, M.L., Spalart, P.R., Strelets, M.K., Travin, A.K., 2008. A hybrid RANS-LES approach with delayed-DES and wall-modelled LES capabilities. Int. J. Heat. Fluid Flow. 29 (6), 1638–1649. https://doi.org/10.1016/j.ijheatfluidflow.2008.07.001.

Spalart, P.R., Allmaras, S.R., 1994. A one-equation turbulence model for aerodynamic flows. La Rech. Aerosp 1, 5–21. https://doi.org/10.2514/6.1992-439.

Spalart, P.R., 2009. Detached-eddy simulation. Annu. Rev. Fluid Mech. 41, 181–202. https://doi.org/10.1146/annurev.fluid.010908.165130.

Wang, Z.Z., Xiong, Y., Wang, R., Shen, X.R., Zhong, C.H., 2015. Numerical study on scale effect of nominal wake of single screw ship. Ocean. Eng. 104, 437–451. https://doi.org/10.1016/j.oceaneng.2015.05.029.

Wu, J.Z., Ma, H.Y., Zhou, M.D., 2006. Vorticity and Vortex Dynamics. Springer, Berlin, Heidelberg.

Wu, P.C., 2013. A CFD study on added resistance, motions and phase averaged wake fields of full form ship model in head waves. Doctoral Thesis. Osaka University, Osaka. http://doi.org/10.18910/26191.